Los Alamos
NATIONAL LABORATORY
memorandum

*Physics Division*
*Plasma Physics (P-24)*

*To/MS:* distribution
*From/MS:* J. A. Cobble
*Phone/Fax:* 7-4879/FAX 5-3552
*Symbol:* P-24-U-99-119

*Date:* 7/30/99 LA-UR-99-4279

**SUBJECT: Ridge and Bump Shock Experiments at Nova**

Radiation-driven hydrodynamics experiments have been performed in planar and cylindrical geometry to test the difference between left-right and axial symmetry. In this memo, we describe the ridge and bump packages, which are mounted in Nova hohlraums, the imaging diagnostic, image analysis, and discuss the resulting data. For information on comparison with calculations, talk with the principal investigator, B. H. Wilde.

The packages are mounted in the midplane of scale 1 Nova hohlraums stretched to 3 mm length. The hohlraum is lengthened to prevent laser light from striking the package. Eight 1-ns square-pulse beams inject ~15 ± 1 kJ to supply the radiation drive while two delayed beams irradiate a Ti foil for backlighting the package at 4.75 keV. The broken 5-fold symmetry of Nova, created by the absence of backlighter beams 7 & 8 from the drive, is corrected by aiming another pair of beams (9, 10) midway into the gap left in the drive. See Fig. 1 below.

Imaging is accomplished with a pinhole camera (PHC) with data recorded on direct exposure film (DEF). As indicated in Fig. 1, the PHC is mounted in SIM-4. We operated in a 200-ps backlighter mode to achieve time resolution. The PHC is equipped with a 4x4 array of 10-μm pinholes to provide multiple, high-resolution exposures, but only for a single time per laser shot. Therefore, several laser shots are needed to accumulate the time-dependent data for shock propagation. Earlier attempts to record data with a gated x-ray detector failed, apparently on account of photon statistics.

Figure 2 shows the PHC view through the Ta radiation shield. Radiation drive is applied from below and impacts a sinusoidal, polystyrene ridge or bump on the bottom of the package. On the ridge targets, the plastic package is cut into

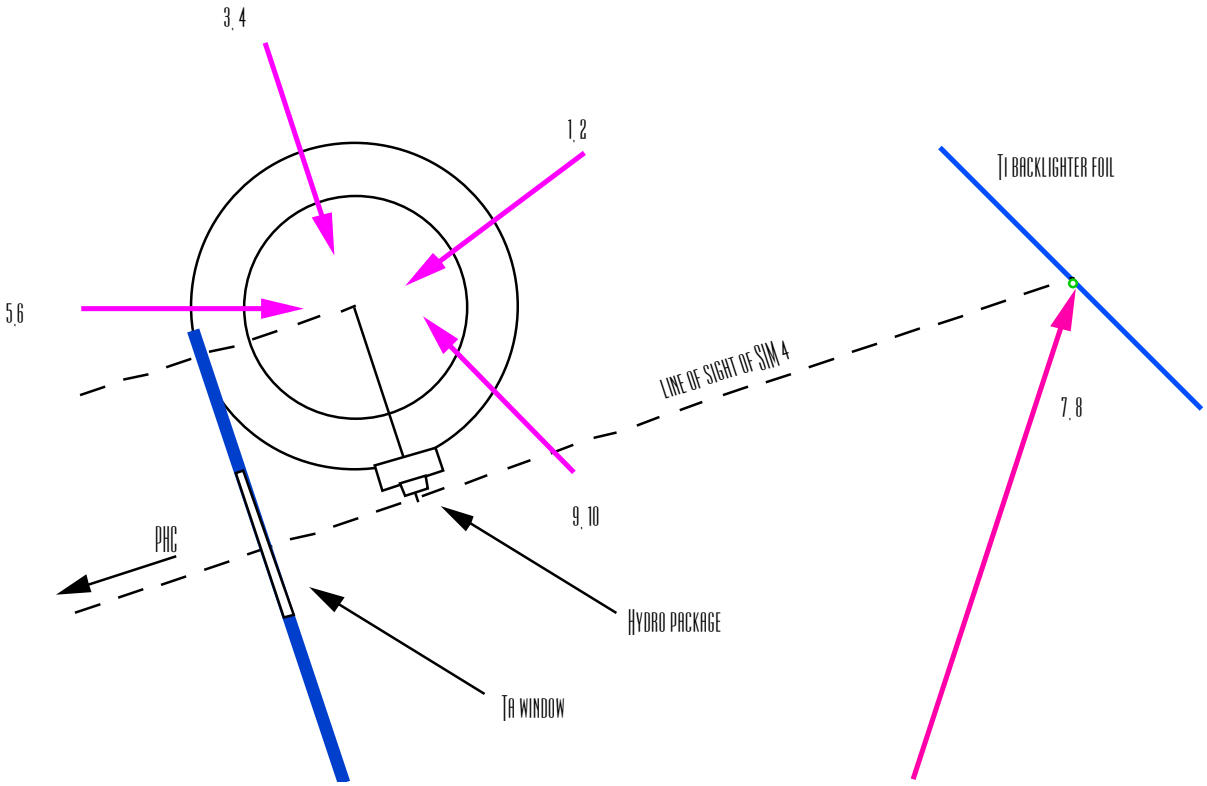


Fig. 1 Scaled drawing of target backlighting of a Nova hohlraum -- The hohlraum diameter is ~1.6 mm. The numbered arrows indicate pairs of Nova beams.

box shapes; for the bumps, all the plastic parts are θ-independent. Since the ridge is viewed from the end, both targets present the same profile to the PHC. The "goal post" in Fig. 2 holds a Au 400-lpi grid used as a spatial fiducial. Because of photon statistics, we find that the images can be improved significantly by adding them together. The fiducials are useful for image alignment in the addition, and we find that this can be done without compromising the PHC resolution.

Data analysis consists of several steps to overlay the images and derive a composite backlighter transmission. The 4x4 PHC film, when scanned, makes a 2000 x 2000 pixel image. We scan using a 20 x 20-μm slit. The numerical aperture

of the densitometer is 0.1. The latter is an essential factor in calculating the film exposure. The primary tasks in analyzing the data are slice & dice, film conversion, frame addition, backlighter model, and calculation of transmission.

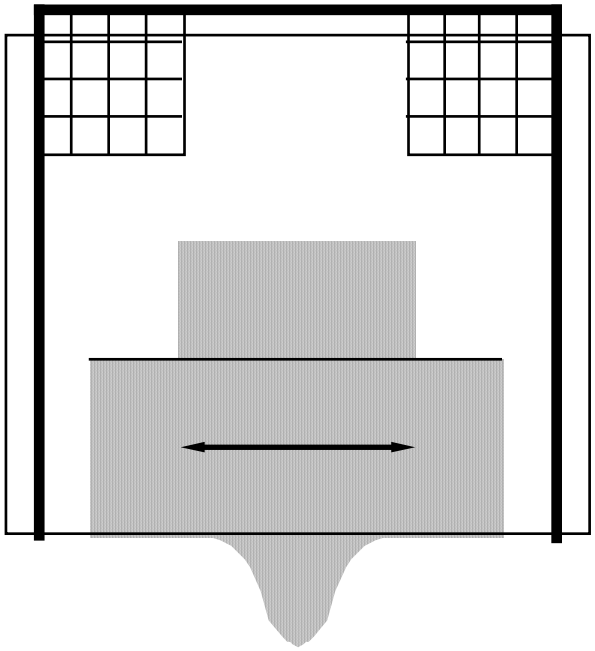

Fig. 2 Line drawing view through the Ta shield window -- The arrow is 400 μm.

Slice & dice refers to creating as many as 16 separate frames, one for each pinhole in the 4x4 array, all with dimensions of 341 x 341 pixels, and each having its fiducial markers aligned within ± ~1 pixel. We have the option of using some or all of the available 16 frames. This is good because not all have equally useful data. One Nova shot was afflicted with "clogged" pinholes, and there were few good exposures.

Next we do film correction. Because of the Ti and Be filtration in recording the data, we assume that the information is carried by the He-like 2-1 transition of Ti. This is the photon energy we use in converting from film density to photons/$\mu m^2$ intensity on the film. An IDL language program is used for the conversion. We have duplicated Henke's exposure table for DEF [J. Opt. Soc. Amer. B, **3**, 1540

(1986)] within ~1%. The differences are due chiefly to improved x-ray absorption coefficients.

Addition is next. Depending on alignment of the PHC, sometimes the four corner frames are partially cut off. A routine exists to add partial frames to the composite image.

Because of the nonlinear nature of film, we elected to average transmissions instead of photon fluxes for the composite image. As it turns out, the weighted average transmission can be modeled successfully by averaging the fluxes and using a composite backlighter model. This is much more user friendly for the analysis and is based on statistical weights of the various frames.

The statistical weight is defined as the reciprocal square of the uncertainty $\sigma$ in a measurement. Thus, for the $i^{th}$ element, in a Poisson regime, the uncertainty is $\sigma = \sqrt{[\ \text{BKLTR}\ ]} / [\ \text{BKLTR}\ ]$ where (bkltr) is the number of photons from the backlighter. Therefore, $(wt)_i = (bkltr)_i$ -- the intensity of backlighter. The weighted average transmission for all the frames in an average is:

$\langle T \rangle = \Sigma\, (wt)_i\, T_i / \Sigma\, (wt)_i$, where the sum is over all the used frames.

Since for the $i^{th}$ frame, $T_i = (data)_i / (bkltr)_i$, this reduces to

$\langle T \rangle = \Sigma\, (data)_i / \Sigma\, (wt)_i = \Sigma\, (data)_i / \Sigma\, (bkltr)_i$.

Therefore, we sum the data and divide by a composite backlighter model. We model the backlighter as an elliptical paraboloid with five fit parameters. The elliptical backlighter pattern on the Ti foil is assumed to be unrotated in the x-y plane. Thus, the equation for the backlighter intensity is:

$I(x,y) = I_0[1 - (x-x_0)^2/a^2 - (y-y_0)^2/b^2]$.

The region for fitting $I_0$, $x_0$, a, $y_0$, and b is taken from the unobstructed portion of the composite image where the transmission is 100%.

To avoid division by zero, we limit the region of analysis arbitrarily to where the backlighter intensity exceeds 5% of its maximum intensity. This accounts for the elliptical shape of the images below. We have also suppressed regions where statistical data fluctuations exceed the backlighter model prediction and have restricted the range of transmission to between 0 - 100% in the displayed images.

The two backlighter beams used in the experiment may not overlap exactly. However, while one could equally well employ a Gaussian or other polynomial function, the paraboloid model is accurate to within ~10% where we can check it. Because of parallax in the 4x4 PHC array, the backlighter hot spot moves from frame to frame. Since the final image is made up of many frames, the structure of the composite backlighter can be biased from one image to the next, depending on the relative light intensity through the various pinholes. This can be seen on the images shown below.

Turning now to the data, we see in Fig. 3 the high-density shocked material in a ridge target propagating through the plastic. The general end-on appearance of the ridge shock shows a smooth dome moving through the plastic. The most distinctive feature is perhaps the “tail” of high density material which follows the leading edge of the shock. It resembles the anatomy of a manta ray and with the dome is suggestive of a devil fish swimming through the plastic. The shoulder of the package coincidentally enhances this illusion. When the dome breaks through corners of the target, the resulting plasma stagnates in vacuum along the symmetry planes at $45^o$ and takes on the appearance of devil’s horns.

The targets, incidentally, whether of ridge or bump variety, usually have some low density fluff on the top of the plastic package. It results from the machining of the targets -- where they were held during the tooling. This accounts for the <100% transmission above the top of this region. It has no effect on the hydrodynamics of the shock front before it reaches that point.

The shock velocity is deduced by measuring the distance of the shock from the machined top edge of the plastic package. Errors in this assessment are due to several factors including: 1) differences in the radiation drive for the three shots, 2) difficulty in determining the plastic-vacuum interface [especially true for 29022520, which suffers from numerous low-light-level frames], and 3) possible differences between the assumed and actual times for the exposures. Of course, it has also been assumed that the shock speed is constant over this time interval. Based on this data, the shock velocity appears to be 30 - 35 μm/ns for the ridge targets. See Fig. 4.

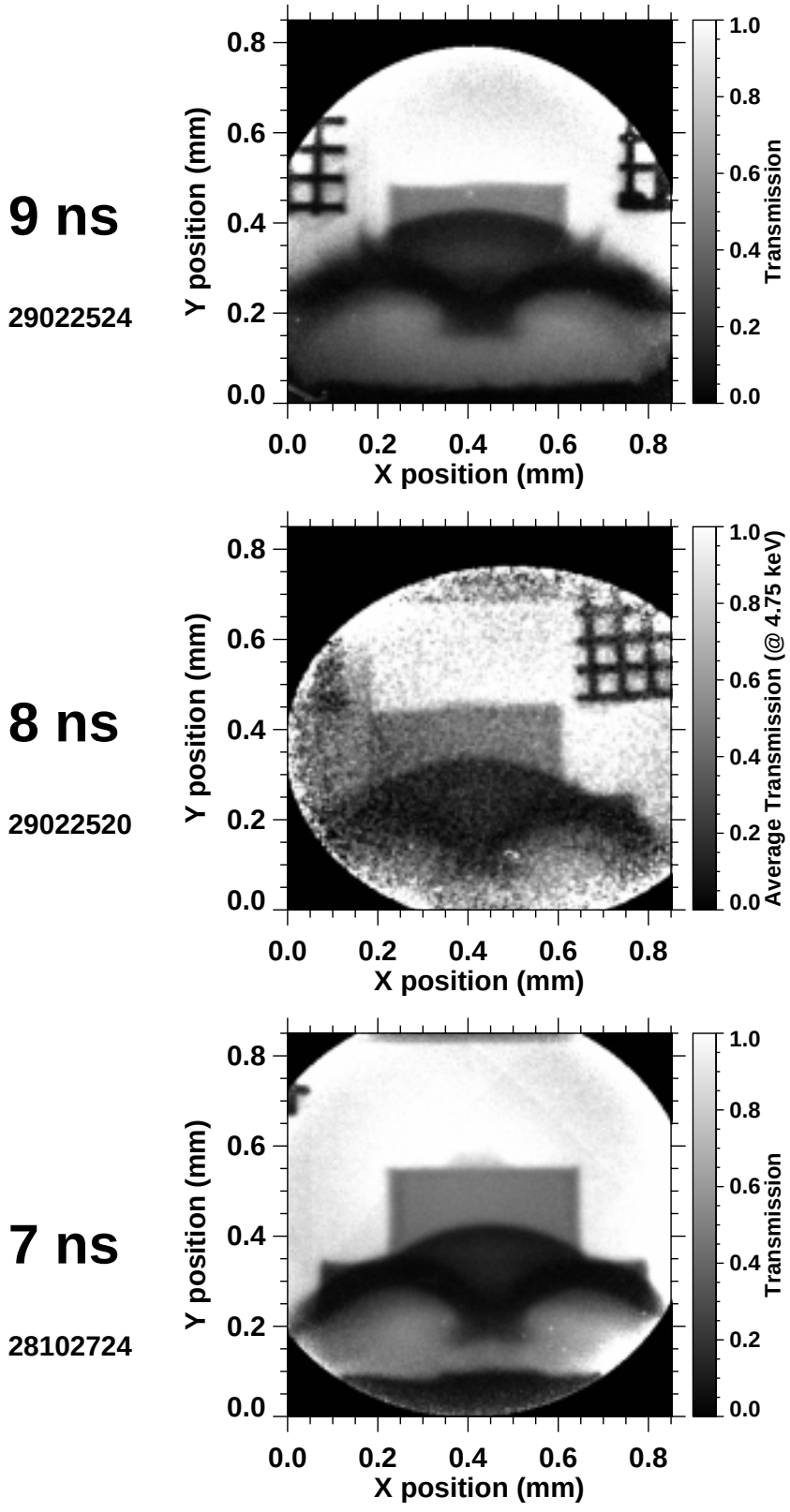


Fig. 3 Propagation of radiation-driven shock through a ridge target

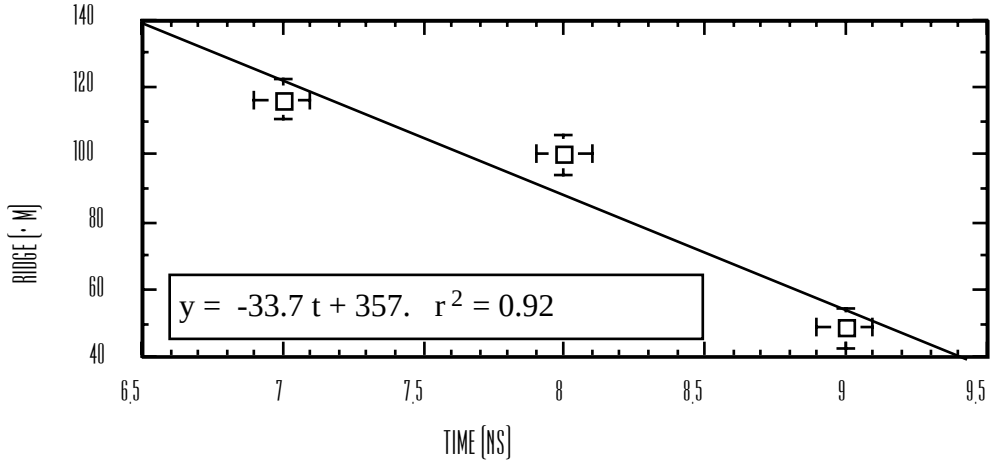


Fig. 4 Shock front propagation history from ridge data in Fig. 3

The bump-target data are shown in Fig. 5. Immediately, we see the difference between the ridge target, in which a shock is launched from the left and right sides of a planar ridge, and the bump target, which is symmetric about the z axis. A thin bubble, evidently on the axis, leads the shock through the plastic. The trailing edge of the shock shows scant sign of a tail, perhaps on account of the lack of integrated opacity near the axis. From examination of the bubble movement through the plastic, we find that it propagates more rapidly than the ridge shock. The constant velocity model seems quite adequate (The data quality is better for the bump targets.) with a shock speed exceeding 40 μm/ns as seen in Fig. 6. The bubble thus moves faster than the ridge shock feature, and this is reasonable since the force of a shock focused from three dimensions is expected to be stronger than a two-dimensional case.

Finally, to do a quality control check, we compare the transmission through an unshocked region of the plastic (from 28102721) with what is calculated from the x-ray opacity of CH at 4.75 keV in a 400-μm diameter cylinder. The linear absorption coefficient used was 21 $cm^{-1}$. We see a rather remarkable fit in Fig. 7, which lends great confidence to the assumptions going into the analysis of the transmission data; namely, that the backlighter intensity is dominated by the

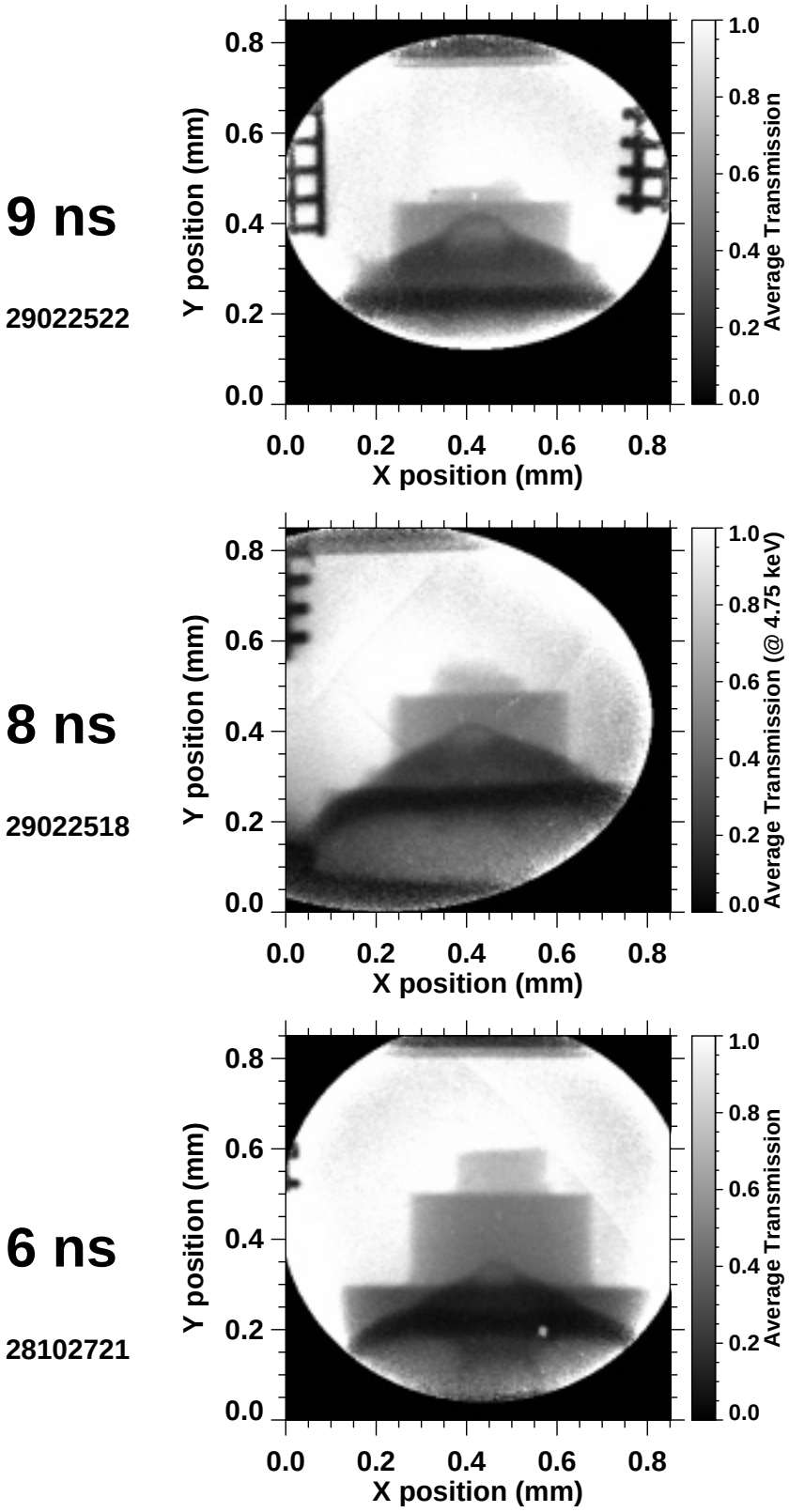


Fig. 5 Propagation of radiation-driven shock through a bump target

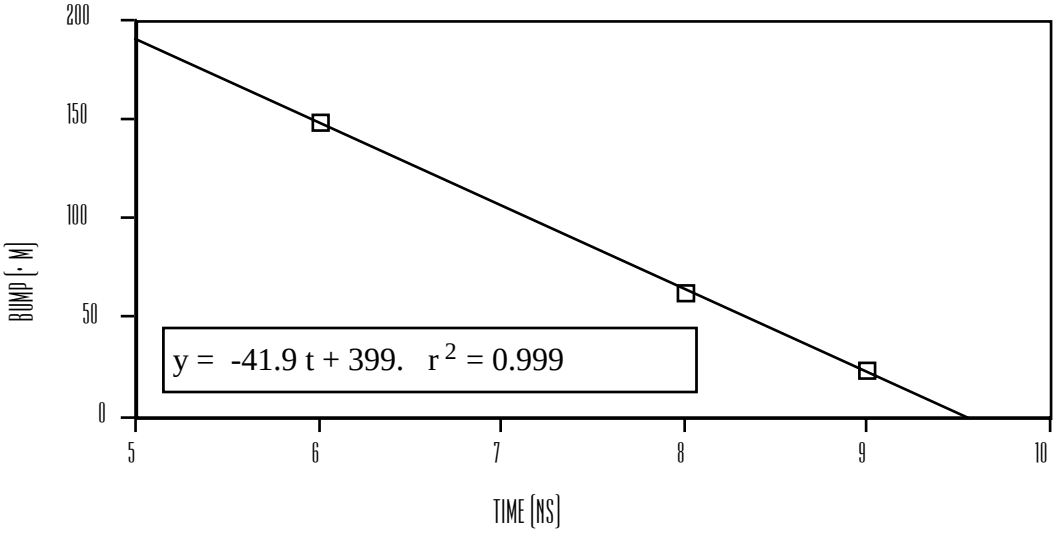


Fig. 6 Shock propagation velocity from bump data in Fig. 5

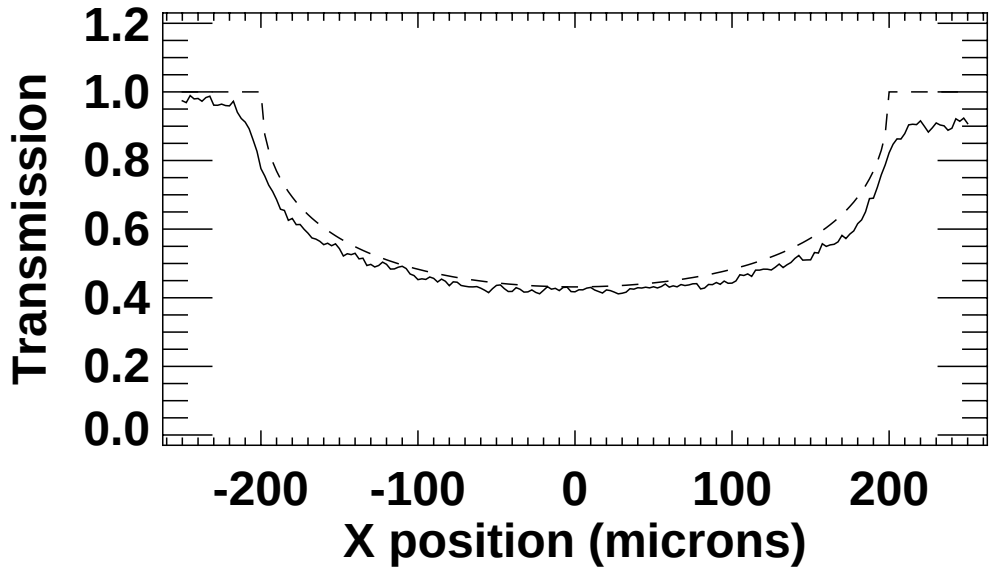


Fig. 7 Comparison of calculated cylinder opacity with measured transmission -- The X position indicates the chord distance from the center of the cylinder. The solid line is the data; the dashes the calculation.

4.75-keV radiation, that the backlighter profile is handled correctly, that the plastic disk is really plastic, really a cylinder, and really 400-μm in diameter.

Steve Caldwell developed many aspects of this experiment in fielding the first data sets. Ken Klare has taken responsibility for numerous IDL analysis codes. John Foster of AWE offered helpful encouragement. As is usual, excellent targets for this experiment were provided by Joyce Moore, Veronica Gomez, and Harry Bush.

Distribution: P-24-U-99-119

| | | |
|---|---|---|
| Hauer Allan | NW-EP | E527 |
| Goldman S. Robert | X-PA | B259 |
| Mason Rodney J | X-PA | B259 |
| Varnum William S. | X-PA | B25 |
| Chrien Robert E. | X-TA | B220 |
| Delamater Norman D. | X-TA | B220 |
| Hollowell David E. | X-TA | B220 |
| Lindman Erick L., Jr. | X-TA | B220 |
| Magelssen Glenn R. | X-TA | B220 |
| Swenson Fritz J. | X-TA | B220 |
| Tubbs David L. | X-TA | B220 |
| Wilde Bernhard H. | X-TA | B220 |
| Wilson Douglas C. | X-TA | B220 |
| Hoffman Nelson M. | X-CI | F663 |
| Caldwell Stephen E. | P-22 | D410 |
| Holtkamp David B. | P-22 | D410 |
| Shlachter Jack S. | P-22 | D410 |
| Watt Robert G. | P-22 | D410 |
| Barnes Cris W. | P-24 | E526 |
| Batha Steven H. | P-24 | E526 |
| Fernandez Juan C. | P-24 | E526 |
| Klare Kenneth A. | P-24 | E526 |
| Kyrala George A. | P-24 | E526 |
| Letzring Samuel A. | P-24 | E526 |
| McLeod John | P-24/AFF | E526 |
| Montgomery David | P-24 | E526 |
| Munson Carter P. | P-24 | E526 |
| Murphy Thomas J. | P-24 | E526 |
| Oertel John A. | P-24 | E526 |
| Paisley Dennis L. | P-24 | E526 |

| | | |
|---|---|---|
| Schappert G. T. | P-24 | E526 |
| Schoenberg Kurt F. | P-24 | E526 |
| Sorem Michael S. | P-24 | E526 |
| Walsh Peter J. | P-24 | E526 |
| Workman Jonathan B. | P-24 | E526 |